Magnetic ground state dependent magnetostriction effects on the chiral magnet CrNb$_3$S$_6$

Masaki Mito [1,2,*], Takayuki Tajiri [3], Yusuke Kousaka [2,4], Jun Akimitsu,[5] Jun-ichiro Kishine,[2,6] and Katsuya Inoue [2,7,8]

[1]*Graduate School of Engineering, Kyushu Institute of Technology, Kitakyushu 804-8550, Japan*

[2]*Chirality Research Center, Hiroshima University, Higashihiroshima 739-8526, Japan*

[3]*Faculty of Science, Fukuoka University, Fukuoka 814-0180, Japan*

[4]*Graduate School of Engineering, Osaka Metropolitan University, Sakai 599-8570, Japan*

[5]*Research Institute for Interdisciplinary Science, Okayama University, Okayama 700-8530, Japan*

[6]*Graduate School of Arts and Sciences, The Open University of Japan, Chiba 261-8586, Japan*

[7]*Graduate School of Science, Hiroshima University, Higashihiroshima 739-8526, Japan*

[8]*Institute for Advanced Materials Research, Hiroshima University, Higashihiroshima 739-8526, Japan*

A prototype of the monoaxial chiral magnet CrNb$_3$S$_6$ exhibited two magnetostriction (MS) effects: (1) spontaneous MS due to the exchange interaction and spin-orbit coupling (SOC) at zero dc magnetic field (H) [Phys. Rev. B **102**, 014446 (2020)] and (2) paramagnetic MS due to SOC and Zeeman energy at room temperature [Phys. Rev. B **105**, 104412 (2022)]. CrNb$_3$S$_6$ has various magnetic structures, such as helimagnetic, first chiral soliton lattice (CSL-1), second CSL (CSL-2), CSL-2 with irreversibility, and forced ferromagnetic phases, resulting from the Dzyaloshinskii–Moriya interaction as a function of H below the magnetic ordering temperature (T_c). In this study, we conducted powder x-ray diffraction analyses to investigate the effects of H and temperature (T) on the MS at the atomic level. The T dependence of the lattice constants reveals that below T_c, the MS depends on the magnetic structure. The MS below T_c is discussed in this study in terms of both the hybridization between the z^2 orbital of Nb($4f$) and delocalized a_1 orbital of Cr and the structural symmetry of the CrS$_6$ octahedron.

I. INTRODUCTION

Crystallographic chirality can be converted into a spin system by the Dzyaloshinskii-Moriya (DM) interaction, which arises from a second-order perturbation between exchange interaction and spin-orbit coupling (SOC) [1,2]. The DM interaction is allowed in a chiral space group without any rotoinversion symmetry elements. Further competition between the DM and exchange interactions results in a long-wavelength spiral order, that is, the helimagnetic (HM) structure, as the magnetic ground state at zero dc magnetic field (H). Magnetostriction (MS), which is common in ferromagnets [3–5], also occurs in the magnetic materials with the DM interaction [6–10] because of a strong magnetostructural correlation originating from the SOC. In a prototype of the chiral magnet CrNb$_3$S$_6$ with a monoaxial DM vector, two types of MS have already been observed: (1) spontaneous MS due to the exchange interaction and SOC at zero H [6] and (2) paramagnetic (PM) MS due to the SOC and Zeeman energy at room temperature [7]. The SOC originates in the hybridization between Cr and Nb [11]. These MS phenomena accompany the change in the interatomic distance between Cr and Nb. Thus these MS effects in CrNb$_3$S$_6$ [6,7] are examples of SOC-induced MS [8–10]. However, MS in CrNb$_3$S$_6$ has not

been thoroughly investigated over wide H and temperature T ranges because of the variation in its magnetic structures.

The monoaxial DM vector in CrNb$_3$S$_6$ results in various magnetic structures below the magnetic ordering temperature (T_c), as shown in Fig. 1(c). In the monoaxial chiral HM structure, the finite H perpendicular to the chiral axis stabilizes a magnetic superlattice called a chiral soliton lattice (CSL), in which the ferromagnetic arrays are connected by kinks called solitons [12–14]. The phase diagram at finite H has been investigated in detail both experimentally [15–22] and theoretically [23–28]. Here, we summarize the phase diagram revealed by these studies. At the surface along the chiral axis, the DM vector is reduced, which stabilizes the forced ferromagnetic (FFM) alignment even at small H [29,30]. The kink (single discommensuration) is a spiral structure with a length corresponding to 2π rotation. Kinks do not disappear at a certain position in the crystal, and they dissipate toward the crystal surface. In thermodynamically stable state, kinks should be arranged periodically such that their rearrangement would apply significant stress to the lattice system, resulting in MS. As H increases, the population of ferromagnetic arrays increases. Consequently, the CSL phase is generally divided into two regions, CSL-1 and CSL-2 [17]. In CSL-1, the surface region has a ferromagnetic alignment at small H, whereas the population of kinks is still larger than that of ferromagnetic arrays. By contrast, in CSL-2, ferromagnetic arrays become more abundant as the solitons in interior of the crystal annihilate by increasing H. This CSL-2 phase is mentioned as

*mitoh@mns.kyutech.ac.jp
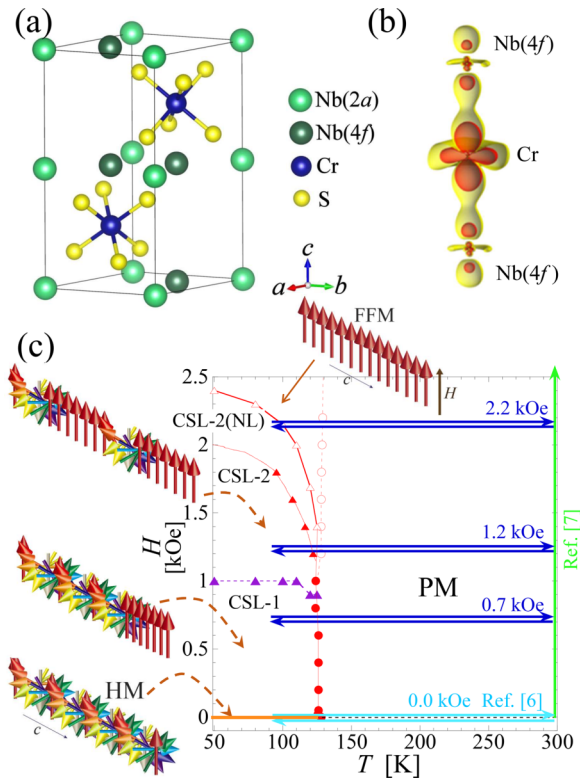
FIG. 1. Characteristics of $CrNb_3S_6$: (a) crystal structure, (b) image of hybridization between $Nb(4f)$ and Cr orbitals, and (c) phase diagram as a function of T and H in bulk single crystal with c-axis length on the order of 0.1 mm [15–22]. The T sequences adopted newly in the present study are illustrated by blue arrows, along with light blue arrow for the T sequence at $H = 0$ Oe in Ref. [6] and green arrow for the H sequence at room temperature in Ref. [7].

inhomogeneous phase in recent study on the phase diagram related with the subject of quantum chromodynamics [31]. As H increases beyond the critical field H_c, the complete FFM state is constructed. Just below H_c, the magnetic hysteresis appears between the processes that increase and decrease H even in bulk crystal. This H region, which is called the nonlinear CSL-2 [CSL-2(NL)] phase, becomes larger with decreasing c-axis length of the single crystal [29,30,32–34]. Thus the magnetic ground state depends on the magnitude of H. Note that the MS effects in $CrNb_3S_6$ are thought to depend on T and H. As mentioned above, in $CrNb_3S_6$, two types of MS have already been observed: (1) spontaneous MS at zero H [6] and (2) PM MS at room temperature [7]. In this study, we experimentally investigate various MS effects as a function of T and H to examine the competition between the DM interaction, exchange interaction, and Zeeman energy in each magnetic ground state.

$CrNb_3S_6$ has a stacked structure of hexagonal NbS_2 layers, as shown in Fig. 1(a). The insertion of localized Cr^{3+} spins between NbS_2 layers excludes inversion symmetry; thus, the material crystallizes as the noncentrosymmetric hexagonal space group $P6_322$ [35–37]. The Nb positions are the $2a$ site with coordinates of $(0, 0, 1/2)$ and $4f$ site with coordinates of $(1/3, 2/3, z)$, which are labeled $Nb(2a)$ and $Nb(4f)$, respectively. All the atomic coordinates of S are general positions.

$Nb(4f)$ is located so that it is in the 3S triangle of the CrS_6 octahedron, and the z coordinate of $Nb(4f)$, $Nb(4f)_z$, is not $1/2$. In this cluster unit, CrS_6-$Nb(4f)$, the local symmetry around Cr is approximately D_{3d}; thus, the Cr $3d$ orbitals exhibit energy splitting $t_{2g} \rightarrow e'_g + a_{1g}$. The z^2 orbital of $Nb(4f)$ is hybridized with the delocalized a_{1g} orbital of Cr, as shown in Fig. 1(b), resulting in the appearance of orbital angular momentum [11].

The T_c value of $CrNb_3S_6$ is reported to be 127 K [17,36,38]. $CrNb_3S_6$ has an HM ground state with a helicity length of 48 nm [36]. According to a Lorenz microscopy experiment, a ferromagnetic network develops on the ab plane [39]. The PM MS at $H//ab$ plane was observed, whereas that at $H \perp ab$ plane was not observed [7]. It has theoretically been investigated that, in the case of monoaxial chiral magnets with large easy-plane anisotropy, CSL state has been observed even when H deviates far from the easy plane, ab plane in $CrNb_3S_6$ [24,26,27]. The existence of CSL in $CrNb_3S_6$ was experimentally confirmed in a wide range of oblique H angles except for when H is closely aligned to the helical axis of the crystal, by magnetic torque and magnetoresistance measurements [18]. Indeed, the PM MS at H with an orientation intermediated between $H//ab$ plane and $H \perp ab$ plane is similar to that observed at $H//ab$ plane [7]. In experiments using a powder sample, we observed the MS distribution in all orientations. Considering the orientation dependence of MS reported in Ref. [7], the MS observed in the powder x-ray diffraction (XRD) data are expected to be characterized as mainly the MS near the $H//ab$ plane direction. The powder XRD experiments are useful for determining all atomic coordinates, which are helpful for understanding MS at the atomic level. Thus we investigated the lattice parameters of the powder sample as a function of T at $H = 0$, 0.71, 1.23, and 2.16 kOe, where the magnetic states below T_c are HM, CSL-1, CSL-2, and CSL-2(NL), respectively. Furthermore, it is noted that at $H = 0$, in addition to spontaneous MS below T_c, no change in all of lattice constants due to competition between the thermal expansion and magnetic shrinkage, so-called the Invar effect, was observed at $T_c < T < 170$ K. There is no change in the Cr–$Nb(4f)$ distance. Below, we focus on (1) the variation of the Invar effect in the PM region characterized by PM MS with H and (2) the variation of SOC-induced MS below T_c with H.

II. METHODS

We performed powder XRD analyses at various temperatures using a synchrotron radiation XRD system with a cylindrical imaging plate at the Photon Factory at the Institute of Materials Structure Science, High Energy Accelerator Research Organization [40]. The energy of the incident x-rays was 16 keV. To produce the maximum H value of 2.2 kOe, two facing NdFeB magnets (NeoMag Co., Ltd.) with remanence value of 13.8 and 14.5 kG were placed in the diffractometer [6]. Because the remanence of the NdFeB magnets depends on temperature, the temperature of the magnets was measured using a K-type chromel-alumel thermocouple. All XRD measurements were conducted under increasing temperature in the range 92.8–294.7 K, and the temperature of the magnets was maintained at 289.2–298.2 K to preserve good
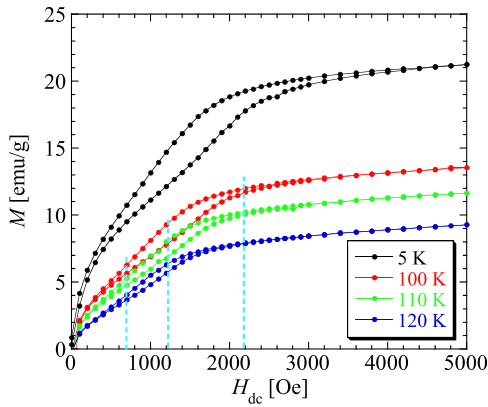
FIG. 2. M-H curve of powder sample of $CrNb_3S_6$ at $T = 5$, 100, 110, and 120 K obtained by magnetization measurements. The light blue broken lines represent the H values adopted in the XRD experiments.

performance. Thus the actual H value at the sample position was calculated as that at room temperature. Figure 1(c) illustrates the series of cooling and warming processes. The powder XRD patterns were obtained during warming after field cooling. The T sequence at $H = 0$ Oe corresponds to PM $\rightarrow$ HM $\rightarrow$ PM, that at $H = 0.71$ kOe corresponds to PM $\rightarrow$ CSL-1 $\rightarrow$ PM, that at $H = 1.23$ kOe corresponds to PM $\rightarrow$ FFM $\rightarrow$ CSL-2 $\rightarrow$ FFM $\rightarrow$ PM, that at $H = 2.16$ kOe corresponds to PM $\rightarrow$ FFM $\rightarrow$ CSL-2(NL) $\rightarrow$ FFM $\rightarrow$ PM.

A powder sample of $CrNb_3S_6$ was synthesized using a procedure described in Ref. [39]. The same powder sample has also been used in a hydrostatic pressure experiment [38,41]; its T_c at $H = 0$ Oe was 127 K. The powders were passed through a sieve with an aperture of 20 μm, and they were held into a capillary with inner diameter of 0.5 mm in the powder XRD experiments. The quality of the Debye-Scherrer ring did not change even under finite magnetic fields, suggesting that the crystallite was not oriented along a peculiar direction there. Indeed, according to Ref. [7], the change in XRD profile for the powder sample seems to trace the influence related to the CSL state stabilized over wide orientation region. The diffraction patterns were analyzed by Rietveld refinement using the RIETAN-FP package [42], where antisymmetric pseudo-Voigt function was adopted.

The H dependence of the magnetization (M) of the powder sample of $CrNb_3S_6$ at $T = 5$, 100, 110, and 120 K was also observed by a commercial superconducting quantum interference device magnetometer. The powder sample held in a plastic capsule had the mass of 12.93 mg. This observation was done to confirm the effects of H at the values used in the XRD experiments.

III. EXPERIMENTAL RESULTS

A. Magnetization measurements

Figure 2 shows the H dependence of M for the powder sample of $CrNb_3S_6$ at $T = 5$, 100, 110, and 120 K. The results confirm magnetic irreversibility between the H increase and decrease processes. The minimum T (5 K) of the M-H measurements is lower than that in the XRD experiment. The

qualitative H dependence observed for the thin crystal is similar to that observed for bulk crystals [29,30,34]. The H region in which irreversibility occurs is known to be narrow in bulk single crystal [32,33], whereas it increases with decreasing the c-axis thickness of single crystal, as described above. Here, let us remember that H_c is 2–3 kOe for $H//ab$ plane (ideal orientation for the stabilization of CSL) and approximately 20 kOe for $H \perp ab$ plane, respectively [36]. In the present powder experiment, the M value at 2.5 kOe corresponds to approximately 70% of the saturation magnetization (29.5 emu/g). This result for the powder sample preferentially reflects the behavior observed in the situation where the CSL is stabilized. Thus the H region depends on the effect of the surface barrier [29,30,34]. In M-H measurements using this powder sample, the feature of CSL observed in the thin crystals was detected. Thus it is considered that the results of the XRD experiment as well as the M measurements could be characterized by those that reflect the construction of CSL state near $H//ab$ plane. The values of $H = 0.71$ and 1.23 kOe correspond to the values required to stabilize the CSL-1 and CSL-2 states, respectively. $H = 2.16$ kOe corresponds to the value required to stabilize the FFM state at 120 K and the CSL-2(NL) state below 110 K. This CSL-2(NL) has small irreversibility between the H increase and decrease processes, whereas it can be considered to be mostly equal to the FFM state.

B. XRD/lattice constants

Figures 3(a), 3(b), and 3(c) show the lattice constants a, c, and the unit cell volume V, respectively, of $CrNb_3S_6$ at $H = 0$, 0.71, 1.23, and 2.16 kOe. Before interpreting the results of this study, we review the changes in the lattice parameters during warming at $H = 0$, which have already been reported elsewhere [6]. In the PM region (130 K $< T <$ 170 K), all of the lattice parameters change very little, suggesting a type of Invar effect due to competition between thermal expansion and magnetic shrinkage. Indeed, ESR signal [43] as well as electrical resistance [15] also change below 170 K, where the exchange interaction would develop. In the HM region ($T <$ 130 K), shrinkage along the a-axis and elongation along the c-axis (chiral axis) occur, and V is almost constant. The reason is that the decrease in volume on the easy plane is canceled by the increase in volume along the hard axis (this change is represented as the increase in the ratio c/a). Thus we consider two phenomena: (1) the PM Invar effect for $T > T_c$ and (2) MS for $T < T_c$ depending on the magnetic ground states.

First, we investigated the PM Invar effect by observing the effect of H on V [Fig. 3(c)]. The Invar effect at the unit-cell level at $T > T_c$ was also observed at $H = 0.71$ kOe, where the T range is almost the same as that at $H = 0$ Oe. The constant V characteristic of the Invar effect was not observed at $H = 1.23$ and 2.16 kOe. At $H = 0.71$ kOe, the surface is FFM and the interior is mostly HM. The HM spin alignment is assumed to stabilize the Invar effect due to competition between thermal expansion and magnetic shrinkage. Further application of H reduces the stability of HM structure, such that, for $T > T_c$, thermal expansion should exceed magnetic shrinkage at $H = 1.23$ and 2.16 kOe.

Next, the MS below T_c at various magnetic ground states was investigated by observing the T dependence of the unit
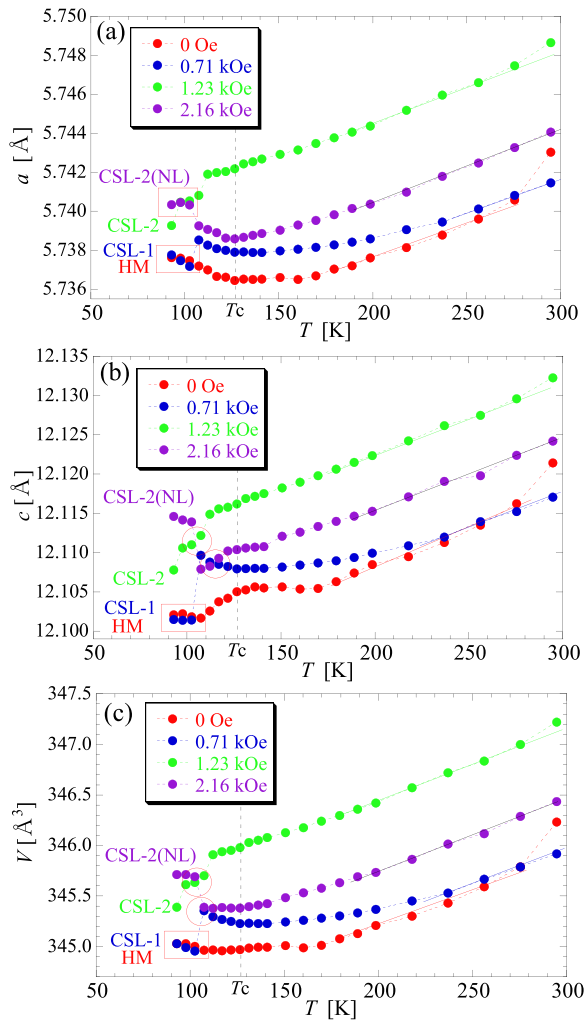
FIG. 3. Lattice parameters (a) a, (b) c, and (c) V estimated experimentally using the powder sample at $H = 0$, 0.71, 1.23, and 2.16 kOe. The position of T_c is represented with a broken line. The qualitative behavior above 200 K, characterized with a straight line, in all of a, c, and V is independent of H. The T region categorized as a group is presented with red rectangle or circle.

FIG. 4. Ratio of c and a, c/a, estimated experimentally using the powder sample at $H = 0$, 0.71, 1.23, and 2.16 kOe. The position of T_c is represented with a broken line.

cell parameters below T_c at various H. According to the lattice constant on the ferromagnetic plane parallel to the magnetic anisotropy vector [$a(T)$ in Fig. 3(a)], the MS at $T < 103$ K can be divided into two categories; the first occurs at 0 Oe (HM) and 0.71 kOe (CSL-1), and the second occurs at 1.23 kOe (CSL-2) and 2.16 kOe [CSL-2(NL)]. The value of a at $T < 103$ K is almost the same at $H = 0$ and 0.71 kOe. At $T = 103$ K, a discretely changes at $H = 0.71$ kOe, and for 107 K $< T < T_c$, the T dependence of a at $H = 0.71$ kOe is similar to that at $H = 2.16$ kOe. At $T < 110$ K and $H = 2.13$ kOe, the T dependence of a is opposite to that at $H = 0.71$ kOe. An increase in a due to MS at $T < T_c$ was observed at 1.23 kOe; it stabilizes the CSL-2 state at $T < 120$ K and FFM state in narrow T region of 120 K $< T < T_c$. The large increase in a during warming occurs in the CSL-2 phase.

Figure 3(b) shows the T dependence of the lattice constant along the hard axis, $c(T)$; the increase at $T < T_c$ and $H = 0$ Oe changes to a discrete increase at 103 K and $H =$

0.71 kOe. Considering the behavior at 93 K, the HM and CSL phases should be placed in the same category, as suggested in the analysis of a, whereas CSL-2 and CSL-2(NL) should be categorized separately. Other features have already been observed in the results for a.

The unit-cell volume V is almost constant at $T < T_c$ and $H = 0$ Oe and just below 103 K at $H = 0.71$ and 2.16 kOe. However, at $H = 1.23$ kOe, the volume exhibits thermal expansion. Because the change in c is much larger than that in a, the T dependence of V below T_c is qualitatively the same as that of c. In addition to a, c, and V, the ratio of c and a, c/a, provides information on the uniaxial distortion of the hexagonal unit cell in the two MS phenomena mentioned above. Figure 4 shows the T dependence of c/a. At $H = 0$ Oe, c/a changes because of MS below T_c and is constant because of the Invar effect at $T_c < T < 170$ K. At $H = 0.71$ kOe, the region of constant c/a resulting from the Invar effect is expanded toward the low-T side, following a discrete change in c/a at T between 103 and 107 K. The Invar effect at both 0 and 0.71 kOe is accompanied by constant c/a, suggesting that the PM Invar effect does not involve the distortion of the hexagonal unit cell. At $H = 1.23$ kOe, c/a is not constant, whereas below T_c, the behavior of c/a is qualitatively similar to that at $H = 0$ Oe. At $H = 2.16$ kOe, the features that appear at $H = 0.71$ and 1.23 kOe are both present, and remarkable changes appear at both 103–107 K and T_c. However, the direction of the change in c/a at 103–107 K is opposite to that at $H = 0.71$ kOe. In summary, above T_c, the behavior of $c/a(T)$ at $H = 0$ Oe is similar to that at $H = 0.71$ kOe; below T_c, the behavior of $c/a(T)$ at $H = 0$ Oe is similar to that at $H = 1.23$ kOe. A first-order-like change was observed below T_c at $H = 0.71$ and 2.16 kOe.

C. XRD/atomic coordinates

It is useful to analyze these phenomena in terms of the atomic coordinates Nb$(4f)_z$, S$_x$, S$_y$, and S$_z$ to understand the origin of MS at the atomic level, as shown in Fig. 5. In particular, Nb$(4f)_z$ [Fig. 5(a)] is an important indicator of hybridization between the z^2 orbital of Nb$(4f)$ and delocalized a_1 orbital of Cr. For reference, under hydrostatic pressure, Nb$(4f)_z$ approaches the z coordinate of Nb$(2a)$, 1/2, owing
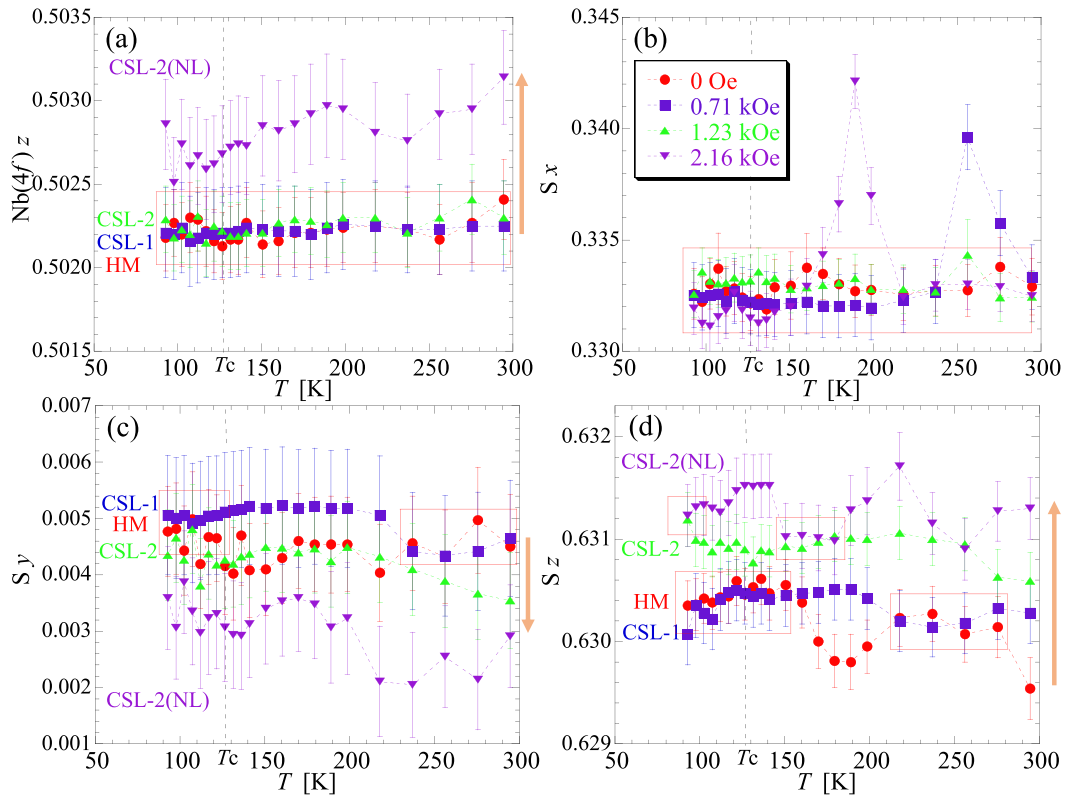
FIG. 5. Atomic coordinates Nb($4f$)$_z$ (a), S$_x$ (b), S$_y$ (c), and S$_z$ (d) estimated experimentally using the powder sample at $H = 0$, 0.71, 1.23, and 2.16 kOe. The position of T_c is represented with a broken line. The T region categorized as a group is presented with red rectangle. Yellow arrows in (a), (c), and (d) stand for trend in the change by increasing H.

to pressurization [38]. Thus thermal shrinkage during cooling clearly differs from contraction under hydrostatic pressure. At $H = 0$ Oe, Nb($4f$)$_z$ exhibits a few characteristic changes, one of which appears at T_c. At $H = 0.71$ and 1.23 kOe, it is different to identify meaningful differences in Nb($4f$)$_z$ compared to that at $H = 0$ Oe because it changes little with respect to the error bars. The values of Nb($4f$)$_z$ for $H = 0$, 0.71, and 1.23 kOe are within 0.5022 ± 0.0001. However, at $H = 2.16$ kOe, Nb($4f$)$_z$ increases to 0.5028 ± 0.0003. At $H = 2.16$ kOe, minima occur at 110 and 230 K. The change in Nb($4f$)$_z$ is discussed in detail below in terms of the change in the interatomic distances Cr–Nb($4f$) to analyze the hybridization between the z^2 orbital of Nb($4f$) and delocalized a_1 orbital of Cr.

Here, let us discuss the possibility of field-induced structural transition. There were observed discrete change in a, c, and V (Fig. 3) at 103–107 K for $H = 0.71$, 1.23, and 2.16 kOe. However, discrete change in c/a (Fig. 4) was not observed at 1.23 kOe. In the data on Nb($4f$)$_z$ [Fig. 5(a)], there was also no discrete change. Similar behavior will be later seen in the data on Cr-Nb($4f$) (Fig. 6). Indeed, there was no qualitative change in a series of XRD pattern. Thus there were observed nondiscrete changes in the atomic level, whereas the change in unit cell volume level exhibits discrete behavior. We cannot mention these phenomena as the so-called field-induced structural transition.

The structural chirality of CrNb$_3$S$_6$ is reflected in the structural symmetry of the CrS$_6$ octahedron. To investigate the change in structural chirality as a function of H, the atomic

position of the lightest atom S in CrNb$_3$S$_6$ must be determined as well. The atomic coordinates of S, S$_x$, S$_y$, and S$_z$, also change at T_c, as shown in Figs. 5(b)–5(d). In particular, at $H = 2.16$ kOe, the change in Nb($4f$)$_z$ appears to be related
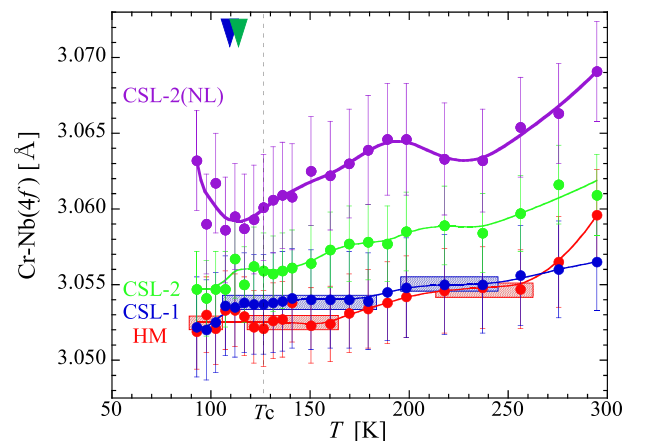
FIG. 6. Interatomic distance Cr–Nb($4f$) obtained experimentally using the powder sample at $H = 0$, 0.71, 1.23, and 2.16 kOe. The meaning of the color of closed circles is consistent with that in Fig. 7. The magnetic states at the lowest T for 0, 0.71, 1.23, and 2.16 kOe are HM, CSL-1, CSL-2, and CSL-2(NL), respectively. Shading indicates the T region of constant Cr–Nb($4f$) distance. Inverted triangles represent the onset temperature at $H = 0.71$ (blue) and 1.23 kOe (green).

with those in S_y and S_z. These results reveal that the MS is related to the change in the atomic coordinates of Nb(f) and S, that is, the symmetry of the CrS$_6$ octahedron (see next section). Both Nb(f)$_z$ and S_z increase with increasing H. The changes in S_x, S_y, and S_z are discussed below in terms of $\angle$S1-Cr-S4 and $\angle$S5-S1-S6 in the CrS$_6$ octahedron.

IV. DISCUSSION

A. Hybridization of Cr and Nb(4f)

The unit-cell MS described above is discussed in terms of the interatomic distance Cr–Nb(4f). Figure 6 shows the T dependence of Cr–Nb(4f), which is the structural parameter most directly related to hybridization between the z^2 orbital of Nb(4f) and delocalized a_1 orbital of Cr, as shown in Fig. 1(b). It is useful to distinguish MS based on the ferromagnetic structure from MS based on the SOC-driven magnetic structures such as HM and CSL structures. At $H = 0$ Oe, thermal expansion in the Cr–Nb(4f) distance occurs as T increases. However, the Cr–Nb(4f) distance tends to remain constant in two regions: below 160 K and 218–256 K. The former T range is very similar to the T range of constant V. At $H = 0.71$ kOe, the two T regions are closer to each other than they are at $H = 0$ Oe. Below 103 K and between 220–250 K, Cr–Nb(4f) has similar values at 0 and 0.71 kOe. When H is increased ($0.71 \rightarrow 1.23 \rightarrow 2.16$ kOe), the Cr–Nb(4f) value increases, suggesting decreased hybridization between Cr and Nb(4f). This result can be understood by considering that the effects of Zeeman energy overcome those of the DM interaction. For $H = 1.23$ and 2.16 kOe, there is no T region in which the Cr–Nb(4f) value is constant. Thus the T dependence of Cr–Nb(4f) differs greatly between the HM-rich phases (HM and CSL-1) and CSL-rich phases (CSL-2 and CSL-2(NL)). For $T < T_c$, a notable increase in Cr–Nb(4f) during warming appears at $H = 0.71$ and 1.23 kOe, which are almost consistent with the changes in c/a. At $H = 2.16$ kOe, it increases continuously with decreasing T. At 110–120 K, the Cr–Nb(4f) values at $H = 1.23$ and 2.16 kOe are quite similar. This increase in Cr–Nb(4f) below 120 K at $H = 2.16$ kOe originates from the stabilization of the ferromagnetic spin alignment forced by H. Thus some features are also evident in Figs. 3 and 4. Inside the crystal, the HM phase is the same as the CSL-1 phase. If the MS at the lowest T below T_c is classified in terms of the atomic coordinates, there are three types of MS: MS based on HM, that based on CSL-2, and that based on CSL-2(NL) with abundant FFM structure. The important terms in the Hamiltonian for each MS are as follows: (1) the exchange and DM interactions in the MS based on HM (corresponding to HM and CSL-1), (2) the exchange interaction, DM interaction, and Zeeman energy in the MS related to CSL-2, and (3) the Zeeman energy overcoming the exchange and DM interactions in the MS at higher magnetic fields. The MS in (1) and (2) originates from SOC, while that in (3) does from the ferromagnetic alignment.

B. Symmetry of CrS$_6$ octahedron

Nb(4f) is located so that it is in the 3S triangle ($\triangle$S4S5S6 in the inset of Fig. 7) of the CrS$_6$ octahedron. The change in Nb(4f)$_z$ leads to the change in the atomic coordinates of S as well as that in Cr–Nb(4f), resulting in the change in
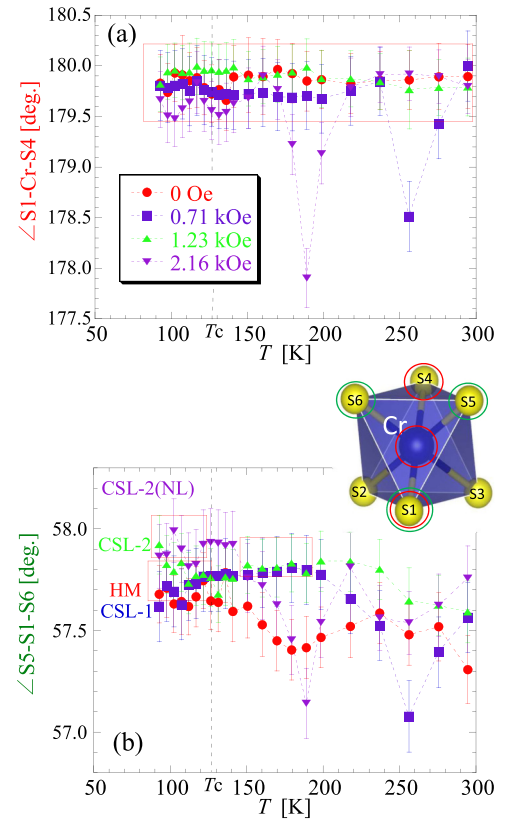
FIG. 7. Atomic angles $\angle$S1-Cr-S4 (a) and $\angle$S5-S1-S6 (b) estimated experimentally using the powder sample at $H = 0$, 0.71, 1.23, and 2.16 kOe. The position of T_c is represented with a broken line. Between (a) and (b), the CrS$_6$ octahedron is illustrated.

the structural symmetry of the CrS$_6$ octahedron. Thus the influence of SOC can be seen in the symmetry of the CrS$_6$ octahedron. The structural symmetry of the CrS$_6$ octahedron can be evaluated using the atomic bonding angles $\angle$S1-Cr-S4 and $\angle$S5-S1-S6. If CrS$_6$ is a true octahedron, $\angle$S1-Cr-S4 $= 180°$ and $\angle$S5-S1-S6 $= 60°$. Figures 7(a) and 7(b) show the T dependence of $\angle$S1-Cr-S4 and $\angle$S5-S1-S6, respectively, at $H = 0$, 0.71, 1.23, and 2.16 kOe. Here, the forced MS effect below T_c is indicated by the changes in $\angle$S1-Cr-S4 and $\angle$S5-S1-S6 as a function of H.

As shown in Fig. 6, at $H = 2.16$ kOe, a large increase in Cr–Nb(4f) compared to that at $H = 0$ Oe was observed, such that the $\angle$S1-Cr-S4 value in the CSL-2(NL) state differs the most from $180°$. However, the $\angle$S5-S1-S6 values in both the CSL-2 and CSL-2(NL) states are closest to $60°$. Thus we should consider the structural symmetry of the CrS$_6$ octahedron from viewpoints of both $\angle$S1-Cr-S4 and $\angle$S5-S1-S6. Indeed, below T_c, the $\angle$S1-Cr-S4 value in the CSL-2 state is the closest to $180°$. According to these analyses, below T_c, CSL-2 has the most symmetric octahedron.

Summarizing the MS at $T \leqslant 103$ K, the lattice constants at $H = 0$ Oe are consistent with those at $H = 0.71$ kOe. Below 103 K, a has similar values at $H = 1.23$ and 2.16 kOe. These relationships are also confirmed in $\angle$S5-S1-S6. However, c and V exhibit different behavior. In the previous subsection, these behaviors have been discussed in the results

of Cr–Nb($4f$) by considering the nature of the HM, CSL, and FFM structures.

The large anomalies in the atomic angles ∠S1-Cr-S4 and ∠S5-S1-S6 at $H = 0.71$ and 2.16 kOe (Fig. 7) are associated with S_x, as shown in Fig. 5(b). The anomalies in the atomic angle ∠S5-S1-S6 at $H = 0$ and 2.16 kOe [Fig. 7(b)] are associated with S_z, as shown in Fig. 5(d). Interestingly, all these anomalies appear in the PM region, and related anomalies do not appear in the unit cell parameters, a, c, c/a, and V.

C. At higher magnetic fields and at lower temperatures

Negative thermal expansion below T_c occurs at $H = 2.16$ kOe. It is explained as the phenomenon by the expansion along with the development of net magnetic moment. Namely, it is considered as an influence due to the ferromagnetism-origin MS. In CSL-2(NL), there is a very small hysteresis in the M-H curve. Thus CSL-2(NL) is a state where the construction of ferromagnetic alignment has almost completed, and it is nearly the FFM state. At higher magnetic fields above 2.16 kOe, there should be also observed the results similar to the result at 2.16 kOe.

At lower temperatures than 90 K, H_c hardly changes according to Refs. [14,17,36]. For instance, the M at $H = 2.5$ kOe for $H//ab$ plane ($H \perp c$) prominently increases down to approximately 50 K [36], suggesting the changes in lattice parameters due to ferromagnetism-origin MS may continue down to approximately 50 K.

V. CONCLUSION

We investigated the MS effects in the typical monoaxial chiral magnet CrNb$_3$S$_6$ by the powder XRD analyses.

Various MS effects are characterized by the Cr–Nb($4f$) distance, which is the quantity most directly related to hybridization between the z^2 orbital of Nb($4f$) and delocalized a_1 orbital of Cr, as well as the lattice parameters. At $H = 0$ Oe, in addition to the PM Invar effect for $T_c < T < 170$ K, constant unit-cell volume also continues below T_c, where the unit cell expands along the c axis during warming as the ab-plane contracts. At $H = 0.71$ kOe, a first-order-like change at the unit cell level appears below T_c. PM Invar effects associated with a constant c/a ratio are observed at H values of both 0 and 0.71 kOe. At $H = 1.23$ and 2.16 kOe, Invar effects do not appear because of the increase in Zeeman energy. The T dependence of the c/a ratio at $H = 1.23$ kOe is qualitatively consistent with that at $H = 0$ Oe, whereas the structural symmetry of the CrS$_6$ octahedron is higher in the CSL-2 phase than in the HM, CSL-1, and CSL-2(NL) phases. At the atomic level, the MS quite below T_c is classified as MS based on HM, that based on CSL-2, and that based on CSL-2(NL) with abundant FFM structure. In CrNb$_3$S$_6$ with SOC, various MS effects were observed, and the actual effects would exhibit various features as a function of both the magnitude and direction of H.

ACKNOWLEDGMENTS

[1] I. E. Dzyaloshinskii, A thermodynamic theory of "weak" ferromagnetism of antiferromagnetics, J. Phys. Chem. Solids **4**, 241 (1958).

[2] T. Moriya, Anisotropic superexchange interaction and weak ferromagnetism, Phys. Rev. **120**, 91 (1960).

[3] A. Katsuki and K. Terao, Magnetovoloume effects of itinerant electron ferromagnets. I. Thermal expansion anomaly of the invar alloy, J. Phys. Soc. Jpn. **26**, 1109 (1969).

[4] M. Shimizu, Magnetovolume effects in itinerant electron ferromagnets, J. Magn. Magn. Mater. **20**, 47 (1980).

[5] S. Khmelevskyi and P. Mohn, Magnetostriction in Fe-based alloys and the origin of the Invar anomaly, Phys. Rev. B **69**, 140404(R) (2004).

[6] T. Tajiri, M. Mito, Y. Kousaka, J. Akimitsu, Jun-ichiro Kishine, and K. Inoue, Spontaneous magnetostriction effects in the chiral magnet CrNb$_3$S$_6$, Phys. Rev. B **102**, 014446 (2020).

[7] M. Mito, T. Tajiri, Y. Kousaka, Y. Togawa, J. Akimitsu, Jun-ichiro Kishine, and K. Inoue, Paramagnetic magnetostriction in the chiral magnet CrNb$_3$S$_6$ at room temperature, Phys. Rev. B **105**, 104412 (2022).

[8] M. Matsunaga, Y. Ishikawa, and T. Nakajima, Magneto-volume effect in the weak itinerant ferromagnet MnSi, J. Phys. Soc. Jpn. **51**, 1153 (1982).

[9] S. Wang, Y. Hu, J. Tang, W. Wei, J. Cong, Y. Sun, H. Du, and M. Tian, Magnetostriction of helimagnets in the skyrmion crystal phase, New J. Phys. **21**, 123052 (2019).

[10] K. Shimizu, H. Maruyama, H. Yamazaki, and H. Watanabe, Effect of spin fluctuations on magnetic properties and thermal expansion in pseudobinary system Fe$_x$Co$_{1-x}$Si, J. Phys. Soc. Jpn. **59**, 305 (1990).

[11] M. Mito, H. Ohsumi, T. Shishidou, F. Kuroda, M. Weinert, K. Tsuruta, Y. Kotani, T. Nakamura, Y. Togawa, J. Kishine *et al.*, Observation of orbital angular momentum in the chiral magnet CrNb$_3$S$_6$ by soft x-ray magnetic circular dichroism, Phys. Rev. B **99**, 174439 (2019).

[12] I. E. Dzyaloshinskii, Theory of helicoidal structures in antiferromagnets. III, Zh. Eksp. Teor. Fiz. **47**, 992 (1964) [Sov. Phys. JETP **20**, 665 (1965)].

[13] J. Kishine, K. Inoue, and Y. Yoshida, Synthesis, structure and magnetic properties of chiral molecule-based magnets, Prog. Theor. Phys. Suppl. **159**, 82 (2005).

[14] Y. Togawa, Y. Kousaka, K. Inoue, and J. Kishine, Symmetry, structure, and dynamics of monoaxial chiral magnets, J. Phys. Soc. Jpn. **85**, 112001 (2016).

[15] Y. Togawa, Y. Kousaka, S. Nishihara, K. Inoue, J. Akimitsu, A. S. Ovchinnikov, and J. Kishine, Interlayer Magnetoresis-

tance due to Chiral Soliton Lattice Formation in Hexagonal Chiral Magnet CrNb$_3$S$_6$, Phys. Rev. Lett. **111**, 197204 (2013).

[16] N. J. Ghimire, M. A. McGuire, D. S. Parker, B. Sipos, S. Tang, J.-Q. Yan, B. C. Sales, and D. Mandrus, Magenetic phase transition in single crystals of the chiral helimagnet Cr$_{1/3}$NbS$_2$, Phys. Rev. B **87**, 104403 (2013).

[17] K. Tsuruta, M. Mito, H. Deguchi, J. Kishine, Y. Kousaka, J. Akimitsu, and K. Inoue, Phase diagram of the chiral magnet Cr$_{1/3}$NbS$_2$ in a magnetic field, Phys. Rev. B **93**, 104402 (2016).

[18] Jun-ichiro Yonemura, Y. Shimamoto, T. Kida, D. Yoshizawa, Y. Kousaka, S. Nishihara, F. J. T. Goncalves, J. Akimitsu, K. Inoue, M. Hagiwara, and Y. Togawa, Magnetic solitons and magnetic phase diagram of the hexagonal chiral crystal CrNb$_3$S$_6$ in oblique magnetic fields, Phys. Rev. B **96**, 184423 (2017).

[19] E. M. Clements, R. Das, L. Li, P. J. Lampen-Kelley, M.-H. Phan, V. Keppens, D. Mandrus, and H. Srikanth, Critical behavior and macroscopic phase diagram of the monoaxial chiral helimagnet Cr$_{1/3}$NbS$_2$, Sci. Rep. **7**, 6545 (2017).

[20] H. Han, L. Zhang, D. Sapkota, N. Hao, L. Ling, H. Du, L. Pi, C. Zhang, D. G. Mandrus, and Y. Zhang, Tricritical point and phase diagram based on critical scaling in the monoaxial chiral helimagnet Cr$_{1/3}$NbS$_2$, Phys. Rev. B **96**, 094439 (2017).

[21] E. M. Clements, R. Das, M.-H. Phan, L. Li, V. Keppens, D. Mandrus, M. Osofsky, and H. Srikanth, Magnetic field dependence of nonlinear magnetic response and tricritical point in the monoaxial chiral helimagnet Cr$_{1/3}$NbS$_2$, Phys. Rev. B **97**, 214438 (2018).

[22] H. Liu, M. T. Trinh, E. M. Clements, D. Sapkota, L. Li, Z. Romestan, S. Bhat, V. Mapara, A. Barua, S. L. Carrera *et al.*, Elastically induced magnetization at ultrafast time scales in a chiral helimagnet, Phys. Rev. B **106**, 035103 (2022).

[23] M. Shinozaki, S. Hoshino, Y. Masaki, J. Kishine, and Y. Kato, Finite-temperature properties of three-dimensional chiral helimagnets, J. Phys. Soc. Jpn. **85**, 074710 (2016).

[24] V. Laliena, J. Campo, Jun-Ichiro Kishine, A. S. Ovchinnikov, Y. Togawa, Y. Kousaka, and K. Inoue, Incommensurate-commensurate transitions in the monoaxial chiral helimagnet driven by the magnetic field, Phys. Rev. B **93**, 134424 (2016).

[25] Y. Nishikawa and K. Hukushima, Phase transitions and ordering structures of a model of a chiral helimagnet in three dimensions, Phys. Rev. B **94**, 064428 (2016).

[26] V. Laliena, J. Campo, and Y. Kousaka, Understanding the $H–T$ phase diagram of the monoaxial helimagnet, Phys. Rev. B **94**, 094439 (2016).

[27] V. Laliena, J. Campo, and Y. Kousaka, Nucleation, instability, and discontinuous phase transitions in monoaxial helimagnets with oblique fields, Phys. Rev. B **95**, 224410 (2017).

[28] Y. Masaki, R. Aoki, Y. Togawa, and Y. Kato, Chiral solitons in monoaxial chiral magnets in tilted magnetic field, Phys. Rev. B **98**, 100402(R) (2018).

[29] M. Ohkuma, M. Mito, N. Nakamura, K. Tsuruta, J. Ohe, M. Shinozaki, Y. Kato, J. Kishine, Y. Kousaka, J. Akimitsu *et al.*, Surface-size and shape dependencies of change in chiral

[30] soliton number in submillimeter-scale crystals of chiral magnet CrNb$_3$S$_6$, AIP Adv. **9**, 075212 (2019).

[30] M. Ohkuma, M. Mito, Y. Kousaka, T. Tajiri, J. Akimitsu, J. Kishine, and K. Inoue, Soliton locking phenomenon over finite magnetic field region in the monoaxial chiral magnet CrNb$_3$S$_6$, Appl. Phys. Lett. **117**, 232403 (2020).

[31] Y. Hidaka, K. Inoue, M. Mito, K. Shigaki, and Y. Yamaguchi (unpublished).

[32] K. Tsuruta, M. Mito, Y. Kousaka, J. Akimitsu, J. Kishine, Y. Togawa, H. Ohsumi, and K. Inoue, Discrete change in magnetization by chiral soliton lattice formation in the chiral magnet Cr$_{1/3}$NbS$_2$, J. Phys. Soc. Jpn. **85**, 013707 (2016).

[33] K. Tsuruta, M. Mito, Y. Kousaka, J. Akimitsu, J. Kishine, Y. Togawa, and K. Inoue, Size dependence of discrete change in magnetization in single crystal of chiral magnet Cr$_{1/3}$NbS$_2$, J. Appl. Phys. **120**, 143901 (2016).

[34] M. Mito, H. Ohsumi, K. Tsuruta, Y. Kotani, T. Nakamura, Y. Togawa, M. Shinozaki, Y. Kato, J. I. Kishine, J. Ohe, Y. Kousaka, J. Akimitsu, and K. Inoue, Geometrical protection of topological magnetic solitons in micro-processed chiral magnets, Phys. Rev. B **97**, 024408 (2018).

[35] F. Hulliger and E. Pobitschka, On the magnetic behavior of new 2H NbS$_2$-type derivatives, J. Solid State Chem. **1**, 117 (1970).

[36] T. Miyadai, K. Kikuchi, H. Kondo, S. Sakka, M. Arai, and Y. Ishikawa, Magnetic properties of Cr$_{1/3}$NbS$_2$, J. Phys. Soc. Jpn. **52**, 1394 (1983).

[37] L. M. Volkova and D. V. Marinin, Role of structural factors in formation of chiral magnetic solition lattice in Cr$_{1/3}$NbS$_2$, J. Appl. Phys. **116**, 133901 (2014).

[38] M. Mito, T. Tajiri, K. Tsuruta, H. Deguchi, J. Kishine, K. Inoue, Y. Kousaka, Y. Nakao, and J. Akimitsu, Investigation of structural changes in chiral magnet Cr$_{1/3}$NbS$_2$ under application of pressure, J. Appl. Phys. **117**, 183904 (2015).

[39] Y. Togawa, T. Koyama, K. Takayanagi, S. Mori, Y. Kousaka, J. Akimitsu, S. Nishihara, K. Inoue, A. S. Ovchinnikov, and J. Kishine, Chiral Magnetic Soliton Lattice on a Chiral Helimagnet, Phys. Rev. Lett. **108**, 107202 (2012).

[40] A. Fujiwara, K. Ishii, T. Watanuki, H. Suematsu, H. Nakao, K. Ohwada, Y. Fujii, Y. Murakami, T. Mori, H. Kawada *et al.*, Synchrotron radiation X-ray powder diffractometer with a cylindrical imaging plate, J. Appl. Cryst. **33**, 1241 (2000).

[41] M. Mito, S. Tominaga, Y. Komorida, H. Deguchi, S. Takagi, Y. Nakao, Y. Kousaka, and J. Akimitsu, Nonlinear magnetic susceptibility measurements at GPa-level pressures, J. Phys.: Conf. Ser. **215**, 012182 (2010).

[42] F. Izumi and K. Momma, Three-dimensional visualization in powder diffraction, Solid State Phenom. **130**, 15 (2007).

[43] D. Yoshizawa, Y. Sawada, Y. Kousaka, J. Kishine, Y. Togawa, M. Mito, K. Inoue, J. Akimitsu, T. Nakano, Y. Nozue, and M. Hagiwara, Anomalous spiked structures in ESR signals from the chiral helimagnet CrNb$_3$S$_6$, Phys. Rev. B **100**, 104413 (2019).